Nanoscale Advances

ROYAL SOCIETY OF CHEMISTRY

PAPER

View Article Online
View Journal | View Issue

Cite this: *Nanoscale Adv.*, 2022, **4**, 3919

Ensemble GaAsSb/GaAs axial configured nanowire-based separate absorption, charge, and multiplication avalanche near-infrared photodetectors†

M. Parakh, R. Pokharel, K. Dawkins, S. Devkota, J. Li and S. Iyer *

In this study, molecular beam epitaxially grown axially configured ensemble GaAsSb/GaAs separate absorption, charge, and multiplication (SACM) region-based nanowire avalanche photodetector device on non-patterned Si substrate is presented. Our device exhibits a low breakdown voltage (V_{BR}) of $\sim -10 \pm 2.5$ V under dark, photocurrent gain (M) varying from 20 in linear mode to avalanche gain of 700 at V_{BR} at a 1.064 μm wavelength. Positive temperature dependence of breakdown voltage ~ 12.6 mV K^{-1} further affirms avalanche breakdown as the gain mechanism in our SACM NW APDs. Capacitance–voltage (C–V) and temperature-dependent noise characteristics also validated punch-through voltage ascertained from I–V measurements, and avalanche being the dominant gain mechanism in the APDs. The ensemble SACM NW APD device demonstrated a broad spectral room temperature response with a cut-off wavelength of ~1.2 μm with a responsivity of ~0.17–0.38 A W^{-1} at −3 V. This work offers a potential pathway toward realizing tunable nanowire-based avalanche photodetectors compatible with traditional Si technology.

Received 7th June 2022
Accepted 10th August 2022

DOI: 10.1039/d2na00359g

rsc.li/nanoscale-advances

Introduction

Near-infrared (NIR) technology has influenced a wide range of technological advancements over the last few decades and has become ubiquitous. With the increasing demand for low light level signal detection in this wavelength range, avalanche photodetectors (APDs) are becoming a cornerstone in a wide range of commercial, military, and research applications, including optical communication, single-photon detection, deep space communication, surveillance, astronomy, autonomous vehicle tracking, and quantum cryptography.[1,2] Planar III–V APDs currently represent state-of-the-art performance in the NIR regime.[4–6] However, their widespread applications are hindered due to their incompatibility with the current CMOS technology stemming from lattice mismatch with Si substrates, high-voltage operation, device scaling challenges, low external quantum efficiency, and the need for external quenching circuits. Nanowires (NWs), due to their one-dimensional architecture and nano footprint in two dimensions, offer unique and distinct attributes, namely enhanced optical trapping, strong nanophotonic resonances, reduced phonon scattering, elastic relaxation of lattice mismatch constraints,[7] ease of material combination along with the implementation of a variety of different architectures providing enormous possible pathways, to address the challenges encountered in the planar configuration. In the APD configuration, NWs offer distinct advantages of low breakdown voltage, low excess noise factor by shrinking the multiplication region to within the dead space thickness, and increased light absorption features over their planar counterparts. Axially configured NWs have the added advantage of high-quality material growth and sharp interfaces that can be exploited to achieve APDs with an exciting figure of merits such as increased probabilistic gain, sensitivity to low photon flux, and small response time. Compared to conventional planar APDs, NW APDs offer the advantage of lower breakdown voltage, and the capability to reduce the dark count rates (DCR) and jitter time. These features are critical in pushing the fundamental limits on higher photon counting rates.

III–V NW APDs have been demonstrated in different configurations. These are InAsP quantum dots embedded in a single InP p–n NW junction with optical avalanche multiplication gain $M > 10^4$ for a single exciton at 40 K under the low operating reverse bias of 8 V,[8] core/shell GaAs p–n NW APDs with surface plasmon-enhanced absorption taking into consideration dead space effect revealing high avalanche gain $M \sim 216$ at −12 V,[9] low-temperature growth of needle-shaped GaAs NW APDs with high multiplication gain $M \sim 263$ at −8 V,[10] separate absorption and multiplication (SAM) region axial InGaAs/GaAs based NW array APDs operating in linear and free-running mode and dark count rates (DCR) below 10 Hz, respectively.[11,12] Similarly, SAM-based single InP/InAsP NW axial

Department of Nanoengineering, Joint School of Nanoscience and Nanoengineering, North Carolina A&T State University, Greensboro, North Carolina 27411, USA. E-mail: iyer@ncat.edu

† Electronic supplementary information (ESI) available. See https://doi.org/10.1039/d2na00359g

heterostructure APDs tuned to 1.55 μm absorption wavelength with gain M up to 12 (ref. 13) and top-down fabricated axial InP NW tapered array APDs demonstrate single-photon detection over broad-bandwidth with external quantum efficiency exceeding 85% (ref. 14) have been reported. Thus, increased multiplication factors with deterministic gain characteristics at lower breakdown voltages (V_{BR}) and broad-spectrum detection of single photons at room temperature (RT) operation have been successfully demonstrated in III–V NW APDs. However, most of the NW APDs are either based on a single NW configuration or arrays grown on patterned GaAs and InP substrates, limiting their integration with present Si technology.

The novelty of this work is the study of GaAsSb/GaAs material system as separate absorption, multiplication, and charge control layer (SACM) APD in the axial NW geometry in the ensemble configuration grown on non-patterned Si substrates. The higher bandgap GaAs as a separate multiplication layer is being used to reduce multiplication noise. GaAsSb has excellent absorption characteristics spanning almost the entire near-infrared (NIR) region, offers ease in bandgap engineering due to the presence of two group V elements, and exhibits high structural phase purity in the NW configuration[15,16] as compared to their traditional InGaAs counterparts.[17] Further, NW growth compatibility with the multiplication layer GaAs makes it an excellent candidate as an absorption region material. The proposed SACM-based structure allows for independent control of electric field intensity in different regions of a single axial NW APD structure. This helps in tuning the absorption region wavelength regime, and breakdown voltage and reduces dark current density, thus decoupling the effective device sensitivity and the target operational wavelength.

Electric field (E-field) simulations guided the device design. Variations in growth temperature during the segment-wise axial growth and shutter sequencing were critical to the successful demonstration of the avalanche mechanism in the axial NW APD device. Temperature-dependent current–voltage (I–V) measurements provided insight into the nature of the breakdown voltage mechanism and enabled optimizing growth conditions to achieve a successful APD device. Further capacitance–voltage (C–V) and low-frequency noise measurements also attested to avalanche characteristics in the NW device. Thus, this work offers a potential pathway for demonstrating next-generation avalanche photodetectors compatible with traditional Si technology and realizing a tunable NW-based APD covering the NIR region.

Experimental

Nanowire simulation

The E-field simulation for the single SACM axial GaAsSb/GaAs heterostructure NW APD was performed using the Semiconductor Module of COMSOL Multiphysics at 300 K.

Nanowire growth

The as-grown ensemble SACM axial NW APDs were grown by self-catalyzed vapor–solid–liquid (VLS) mechanism using molecular beam epitaxy (MBE) on non-patterned n-Si<111> substrates. The NW growth was initiated with a 10 s Ga flux before opening the group V fluxes to initiate Ga catalyzed epitaxial NW growth at the pyrometer substrate temperature of 607 °C. The Sb_2 and As_4 flux were provided by valved cracker sources operating at 900 °C and 600 °C, respectively. Group V/III flux ratio of 10 was used, with an As/Sb ratio of 5 resulting in Sb incorporation of ∼7 at% (ref. 18–21) in the absorption region. GaTe and Be source materials were used for segmental doping at 540 °C and 925 °C, yielding n-type doping $\sim 10^{18}/cm^{-3}$ and p-type doping $\sim 5 \times 10^{17}/cm^{-3}$,[22] respectively. A p^+-contact layer with Be cell temperature of 925 °C and a group V/III flux ratio of 10 was used for ∼4 at% Sb incorporation in the segment. NW APD core growth was terminated using As_4 flux to consume the Ga-catalyst droplet present on the NW tip, and the substrate temperature was ramped down to 465 °C for surface passivation. The NW APD core was passivated using vapor–solid (VS) growth of GaAlAs shell for 7 min followed by a thin GaAs shell ∼ 2 min to prevent Al oxidation. The individual axial segment growth rates were calculated from SEM images performed on segment-wise axial APD structure growth, as explained in ESI S6.†

Nanowire device fabrication

SU-8 polymer was spin-coated on as-grown ensemble NW APDs. The excess polymer was etched using reactive ion etching to expose the NW tips before the chemical treatment[23] to remove the GaAlAs passivation layer. Silver (Ag) NWs and silver paste served as top and bottom contacts of the NW APD device, respectively. A schematic of the NW device fabrication process is shown in Fig. 1.

Characterization tools

The morphological properties of NWs were assessed using the Carl-Zeiss Auriga-BU FIB field emission scanning electron microscope (FESEM).

Micro-photoluminescence (μ-PL) system used for the assessment of the optical properties of NW APDs, comprised of a 633 nm He–Ne laser as the excitation source, 0.32 m double grating monochromator for the wavelength dispersion, and an InGaAs detector with conventional lock-in techniques. A closed-cycle optical cryostat from the Montana cryostat with the sample chamber interfaced with a fiber-coupled confocal microscope captured the 4K PL spectra.

The current–voltage–temperature (I–V–T) characteristics of ensemble NWs were obtained using two probe Keithley-4200 semiconductor parameter analyzer systems integrated with a radiation shield equipped Lake Shore TTPX probe station. A microHR (LSH-T250) Horiba spectrometer equipped with a tungsten-halogen lamp excitation source was used with an optical illumination area of 2.25×10^{-4} m^2 for studying the device photoresponse. The computation of device responsivity is discussed elsewhere.[24] The I–V characteristics of the NW APD device were measured by limiting the current compliance of the measurement system to 10^{-4} A, as the NW APD devices were found to degrade during the operation at higher current conduction (ESI S5†).

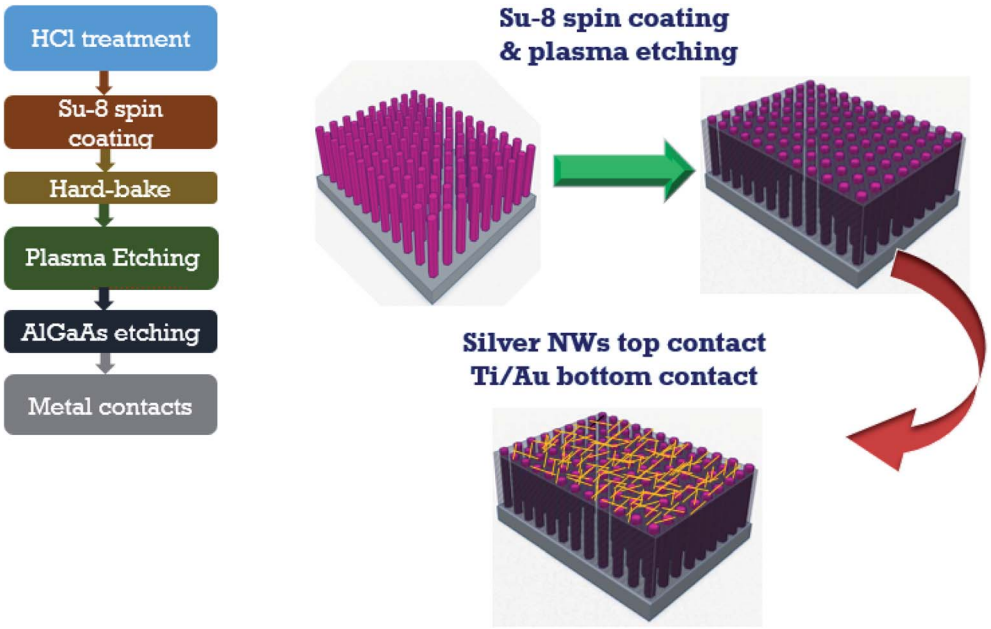

Fig. 1 Schematic process of NW APD device fabrication following epitaxial growth by MBE.

The capacitance–voltage (C–V) measurement was performed using a Keithley source meter with the incremental change in the voltage by 30 mV.

Finally, Keysight 35670 dynamic signal analyzer equipped with two independent low noise current preamplifiers was used for low-frequency noise measurements. The source-drain bias was provided by the internal batteries of these two amplifiers, and its output terminals were connected to two different channels of the dynamic signal analyzer. Measurements were carried out from 10 Hz to 3200 Hz, and the data were averaged over 500 sets of readings.

Results and discussions

SACM axial NW APD schematic and electric field simulation

Fig. 2(a) illustrates the schematic of the single SACM axial GaAsSb/GaAs heterostructure NW APD passivated with lattice-matched GaAlAs layer to mitigate the Fermi level pinning effect caused by surface states.[25] The radial dimension of the single NW structure was ~110 ± 5 nm (measured over 50 NWs) based on the SEM measurements of the optimized initial n-GaAs NW core segment growth on the n-Si<111> substrate. The choice of the SACM structure is to exploit the NIR absorption tuning of GaAsSb material with Sb composition and reduce band-to-band tunneling in the higher bandgap GaAs multiplication region. The band alignment under zero and reverse bias for the proposed SACM NW APD structure is shown in Fig. 2(b), where the i-GaAsSb absorption region segment is separated from the i-GaAs avalanche multiplication region to suppress the carrier tunneling component.

COMSOL Multiphysics software was used to study the E-field variation in the proposed NW structure for different segment thicknesses and served as an initial guide to structure design. For simulation purposes, all the surfaces were treated as non-ideal. The list of material parameters used in the simulation is provided in Table I (ESI S1†). From simulation analysis (ESI S2†), the multiplication region thickness and charge control region doping variations were identified as the two critical parameters that have pronounced effects on modulating the E-field distribution throughout the NW APD structure. Reduction in the multiplication region thickness led to E-field intensity enhancement (Fig. S2(a)†) for a given charge control layer doping.[26] Increasing the charge control layer doping resulted in a further increase in graded E-field distribution across the NW device but at the expense of higher operating avalanche breakdown voltage (V_{BR}). Increased doping in the charge control layer is also likely to promote tunneling current from the absorption region at a higher reverse bias leading to a large dark current.[27] Hence, based on simulation results, an optimum doping value of ~5×10^{17}/cm^{-3} in the charge control layer and multiplication region thickness of ~200 nm was selected to yield low V_{BR} ~ −10 V. In addition, a smaller multiplication region would favor deterministic gain characteristics due to increased dominance of dead space effect.[9] Fig. 2(c) shows the E-field contour plot generated at −10 V exhibiting high E-field > 5×10^5 V cm^{-1} (required for avalanche breakdown in GaAs system) in the multiplication region based on the optimized schematic of the single SACM axial NW APD simulation results. This shows that carriers can attain saturation velocity before entering the multiplication region with a marginal graded E-field distribution in the charge control region, enhancing probabilistic impact ionization.[3]

Nanowire growth optimization

This section discusses unique approaches to mitigating different axial NW growth-related issues to reach optimized

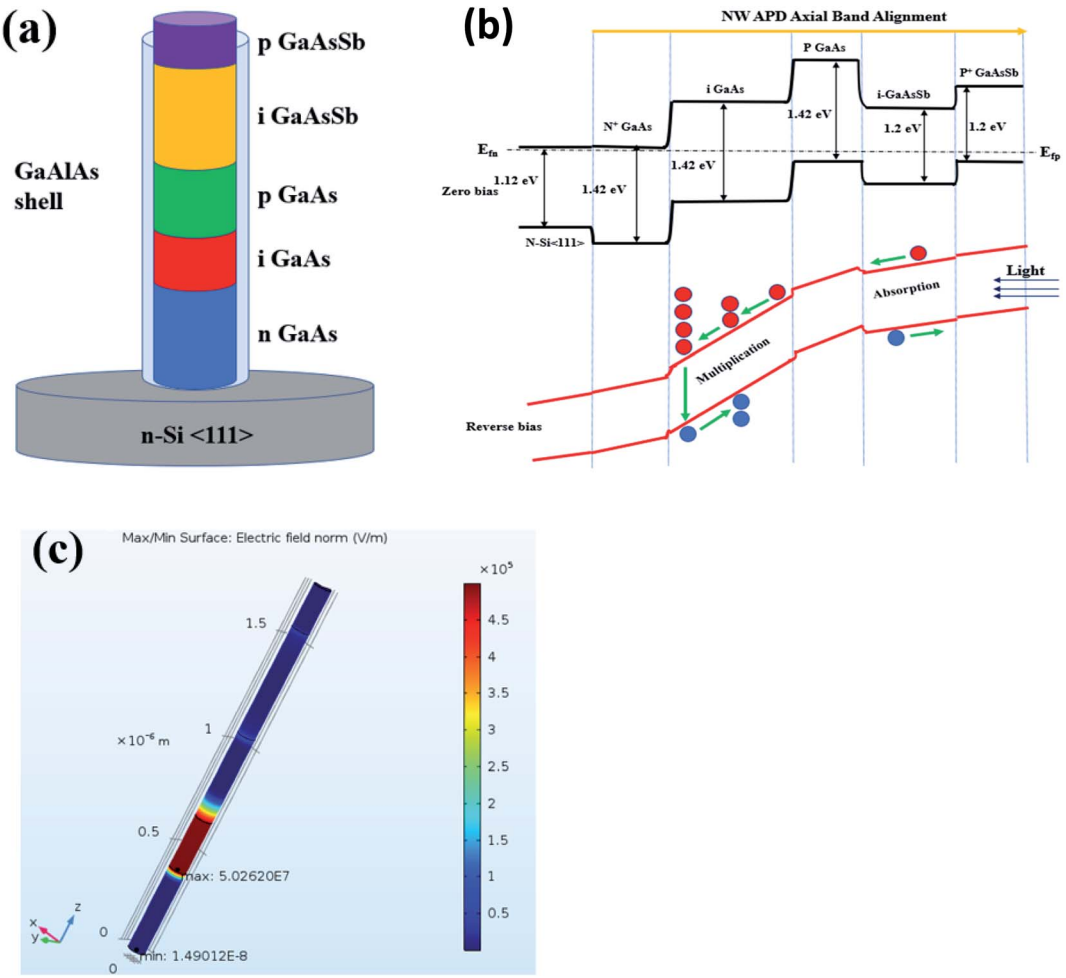

Fig. 2 Single SACM axial NW APD (a) schematic, (b) band diagram under zero and reverse bias operations, and (c) *E*-field distribution plot at −10 V.

growth conditions that promote the avalanche mechanism in the NW structure.

First, the growth of charge control p-doped GaAs NW segment with efficient Be-incorporation and minimum inter-segmental dopant diffusion is essential. It is reported that the deactivation of Be-dopant occurs in GaAs NWs grown under an As-rich environment due to the formation of stable surface As_{Ga} (As antisite) defects. These defects are responsible for Fermi level pinning[28] at the NW surface, causing an electron accumulation layer. This intrinsic limitation was suppressed by reducing As_4/Ga flux ratio to half[28,29] of those used in the other n and i-segments growth. Further Be-dopant diffusion from charge control GaAs layer to multiplication layer, can cause tunneling mechanism to dominate (Zener breakdown) and result in internal gain variation in axial NW configuration. To reduce Be-dopant diffusion from the charge control segment in the underneath i-GaAs multiplication segment, Be shutters were opened and closed for a few seconds for the first few cycles of the p-GaAs growth.

Second, the growth of GaAsSb material system of the uniform diameter as that of underlying GaAs structure is another critical optimization feature, requiring judicious selection of growth parameters. Sb is a well-known surfactant,[30] aiding lateral overgrowth and inverse tapering of the NWs (which can lead to early growth termination and undesirable shell growth[31,32]). These can create a potential shunt path for carriers generated in the absorption region due to thin radial shell growth. An increase in substrate temperature by 3 °C at the start of GaAsSb segment growth suppressed the radial shell growth, hence minimizing the shunt current path (inset SEM image of optimized single axial NW APD (Fig. 2(a))). The substrate temperature was subsequently lowered by 5 °C during the growth for enhanced Sb incorporation.

Lastly, as the top p^+ GaAsSb contact layer determines the light absorption characteristics of the axial APD device, a higher bandgap layer consisting of lower Sb composition with an optimum thickness of ∼300 nm was used. It is important to note that numerous unoptimized NW APD growths resulted in devices exhibiting soft-knee Zener breakdown (shown in ESI S3†) before arriving at the optimized recipe for ensemble SACM axial NW APD structure, revealing the importance of optimized structure growth.

SEM and photoluminescence (PL)

The free-standing ensemble SACM axial GaAsSb/GaAs NW APDs growth under optimized conditions yielded high-density vertical NWs on n-Si<111> substrate, as shown in the SEM image of Fig. 3(a). The self-catalyzed growth with the passivating shell exhibited an average NW length of $\sim 1.8 \pm 0.12$ μm and an average diameter of $\sim 110 \pm 5$ nm (measured over 50 NWs). The SEM image of a single NW APD core (inset of Fig. 3(a)) without droplet consumption demonstrates the realization of uniform NW APD diameter under optimum growth conditions.

The 4K-PL spectra of the NWs in Fig. 3(b) reveal two prominent peaks at 1.28 eV and 1.48 eV, corresponding to the compositions of GaAsSb in the absorption and GaAs segments, respectively. A broad FWHM $\sim$ 0.34 eV of GaAsSb spectra and a lack of sharp low energy onset suggest the presence of defects, generally attributed to acceptor vacancies in the intrinsic-Sb material system.[33]

Current–voltage (*I–V*) measurements

Multiple RT *I–V* sweeps under dark were performed on the ensemble SACM axial NW APD device samples, as shown in ESI S4.† Under reverse bias operation, a low dark current from 10 pA to 100 pA was observed before the onset of breakdown at $\sim -10 \pm 2.5$ V, where the current increased sharply by 3 to 4 orders of magnitude, a signature of avalanche breakdown.[34] Repeated *I–V* sweeps shifted the V_{BR} from −10 V to −7.5 V, which became stable. The range of V_{BR} obtained was consistent with those computed based on the *E*-field simulation of this structure, as discussed earlier in the simulation section.

Under 1.064 μm illumination, the *I–V* characteristics of the NW APDs displayed low photocurrent at zero bias, indicative of incomplete depletion of the absorption region (Fig. 4(a)). With increased reverse bias, a surge in photocurrent was observed at ~ -2 V, which plateaued at −3 V. This is a typical signature of punch-through voltage or unity gain point[35] corresponding to the depletion region extending to the absorption region edge. Therefore, −3 V was considered the unity gain (UG) point providing a conservative estimate to avoid overestimating the gain in our NW APDs. On illumination, the V_{BR} shifted further to a lower bias of ~ -6 V and remained invariant in the subsequent scans under both dark and light. This shift towards lower V_{BR} during the initial sweeps under both dark and illumination is speculated to be any or all of the following. (a) Annihilation or redistribution of traps during the repeated sweep and illumination reaching a steady state of trap density thereafter and (b) the formation of a secondary electric field within the NW device due to pinning of the Fermi level at depletion region edge (formed in absorption region) at the polymer (SU-8 in this case) surface where NW tips are exposed.[36] Both of these possibilities can aid in achieving the required *E*-field necessary for premature avalanche breakdown at a comparatively lower reverse bias than expected from the simulation results discussed earlier. It is noteworthy that the V_{BR} range obtained in our NWs is consistent with other III–V APD reports, namely p–n core/shell GaAs nanoneedle APDs,[10] p–n core/shell GaAs NW APDs,[9] SAM InGaAs NW APDs,[11] and GaAs thin-film homojunction APDs.[37]

Gain (M) calculated using McIntyre's equation:[38] Gain $(M) = (I_{ill} - I_{dark})/(I_{ill} - I_{dark})_{UG}$ revealed a monotonous increase from $\sim$20 just below V_{BR} (Fig. 4(b)) to $\sim$700 after V_{BR} as depicted in the inset of Fig. 4(b) for our as-grown ensemble APDs.

The presence of the avalanche mechanism in these devices was further corroborated by the temperature-dependent *I–V* measurements under dark (Fig. 4(c)). A positive V_{BR} coefficient $\sim +12.6$ mV K^{-1} in the temperature range of 77–300 K was noted with distinct sharp breakdown characteristics under dark, attesting to a band-to-band avalanche mechanism.[39] The low value of the temperature-dependent V_{BR} coefficient suggests the dominance of the dead space effect in our NW APDs. It is ascribed to the thin multiplication region thickness of $\sim$200 nm in our NW APDs. Further, a higher device testing temperature of 350 K yielded a significant rise in current due to increased background thermal carrier generation and carrier tunneling, thereby terminating the avalanche process in the NW APDs. Current saturation observed at both the extremum of reverse and forward bias voltages is due to testing instrument compliance discussed in the Experimental section.

A broad spectral response was observed for the ensemble SACM axial NW APDs, covering visible to the near-infrared region with a cut-off around 1.2 μm (Fig. 5(a)). The maximum response of $\sim$1.064 μm is consistent with the PL peak energy (Fig. 3(b)) corresponding to the GaAsSb absorption segment. The power-dependent excitation study (using 30 mW 633 nm laser at RT in Fig. 5(b)) at a low reverse bias of −1 V displays an

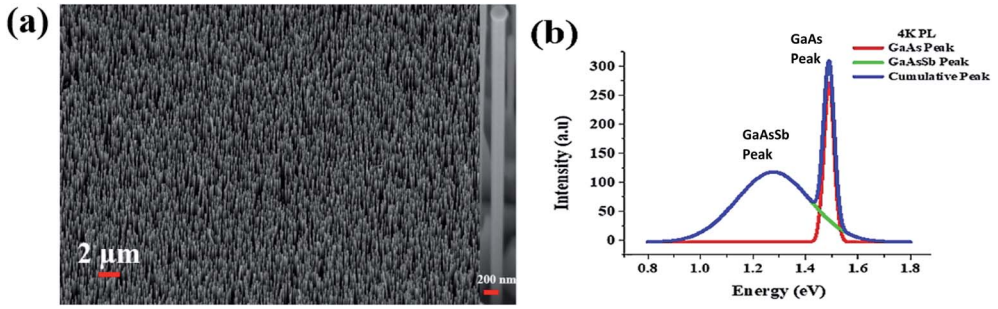

Fig. 3 High-density as-grown ensemble axial SACM NW APDs (a) SEM image of NW APD growth on n-Si<111> (inset: single NW SACM APD core), and (b) 4K PL spectra.

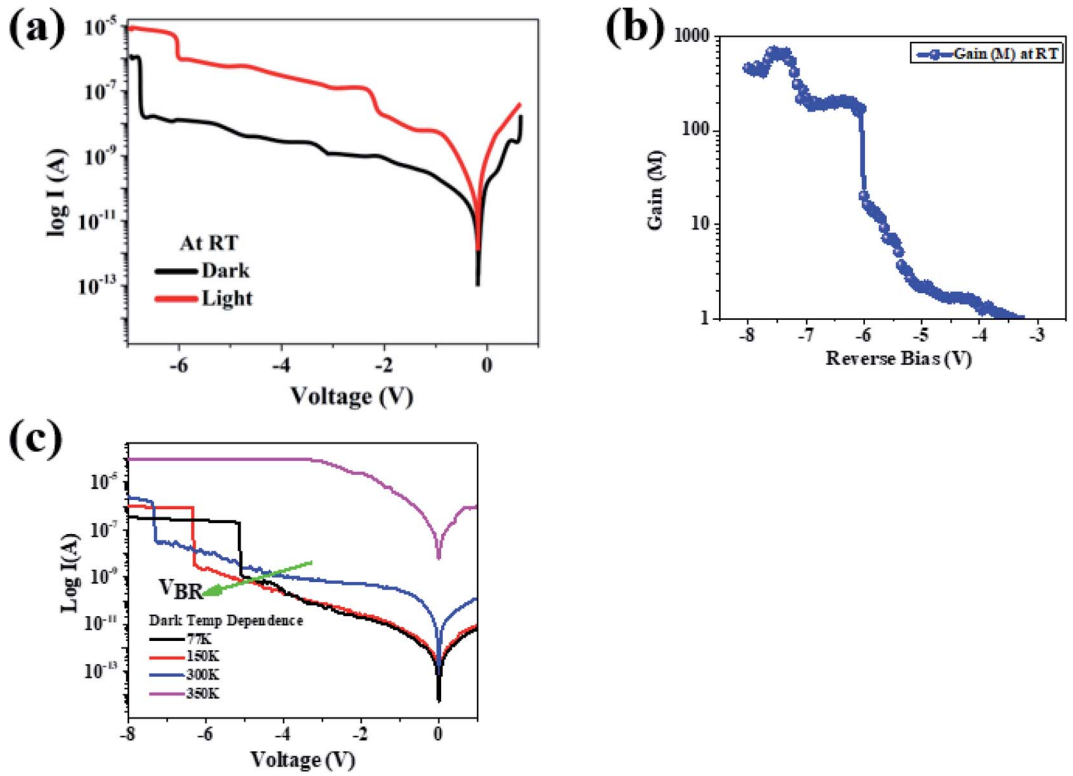

Fig. 4 Ensemble SACM axial NW APD device (a) I–V characteristics at RT under dark and light, (b) gain under illumination with increasing reverse bias, and (c) temperature dependence of V_{BR} from 77 K to 350 K using I–V–T characteristics under dark.

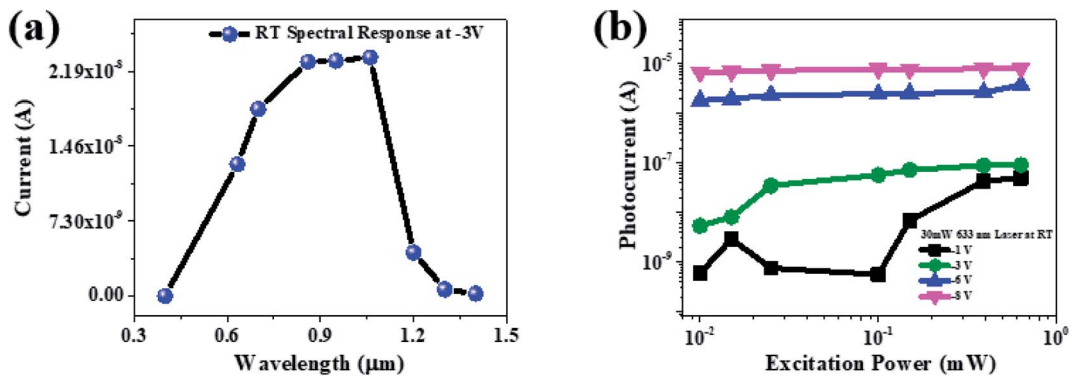

Fig. 5 Ensemble SACM axial NW APD device: (a) spectral response at punch through voltage ~ −3 V, with an illumination power of ~5 mW, and (b) laser excitation power dependence at RT for different reverse bias.

S-curve behavior, characteristic of trap filling.[40] The invariant behavior of photocurrent with excitation power at a higher reverse bias of −6 V and −8 V further confirms the avalanche breakdown mechanism under illumination at −6 V, as discussed earlier in this section.

C–*V* measurements

The RT 1 MHz *C*–*V* characteristics of the ensemble SACM axial NW APDs (Fig. 6(a)) under 1.064 μm illumination exhibit a low capacitance of ~1 pF up to −3 V followed by a monotonic decrease with increasing reverse bias up to −6 V. Under illumination, capacitance is independent of reverse bias increasing from −1 V to −3 V, attributed to the depletion width expansion being offset by the optical generation of charge carriers. With a further rise in reverse bias, the capacitance value declined rapidly and saturated at ~0.67 pF beyond −6 V, signifying complete depletion of NW APD structure corresponding to avalanche breakdown voltage.

A *C*–*V* measurement study was performed at a range of frequencies, as shown in Fig. 6(b), to ascertain the presence of any interface trap states, as these influence the ability of the carriers to follow the AC signal. At 1 MHz, a low capacitance of ~0.3 pF is consistent with the small footprint of the NWs. It is representative of the geometrical capacitance associated with

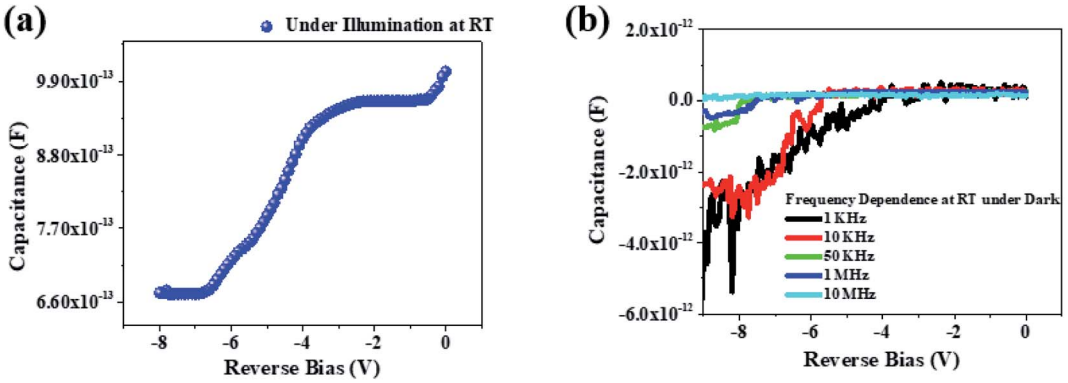

Fig. 6 Ensemble SACM axial NW APD device (a) RT capacitance *versus* reverse bias characteristics under illumination, and (b) capacitance *vs.* frequency dependence under dark.

the absorption and the multiplication regions. The negative capacitance observed at lower frequencies very likely originates from the accumulation of charge carriers at the interface and/or charging/discharging of the traps arising from the impact loss process, where excess energy gained by electrons in the high *E*-field knock-off electrons trapped in the states below the Fermi level.[41] Also, it is to be pointed out that at lower frequencies, the impedance associated with the capacitance becomes so large that the values are not representative of the true capacitance value. However, the trend in the onset of the negative capacitance occurring at a lower bias region with lower frequency is indicative of the probing of larger trap cross section. However, under illumination, the negative capacitance was not as pronounced at lower voltages suggesting the traps were being filled by the photocarriers.

Noise measurements

Low-frequency noise spectroscopy (LFN) of NW APD at RT under illumination (Fig. 7(a)) exhibited a noise power spectral density (PSD) roll-off after 10 Hz till 40 Hz for a reverse bias variation from −1 V to −6 V. All the PSD curves follow a Lorentzian fit (not shown here) at a lower frequency, suggesting the dominance of generation–recombination noise due to the presence of traps, which are consistent with the broad 4K-PL spectral line shape for GaAsSb related peak and *C*–*V* measurements discussed earlier. Beyond the corner frequency of 40 Hz, frequency-independent white noise was observed. A sharp rise in the noise floor by ∼2 orders of magnitude at −3 V and again at −6 V correlates well with the additional noise contribution at punch through voltage caused by the maximum generation of carriers in the absorption region and carrier multiplication at the onset of avalanche mechanism, respectively.

The temperature-dependence of noise under dark at 77 K for an applied bias of −5 V (Fig. 7(b)) reveals significant suppression of generation-recombination noise at low frequency with overall noise floor increased compared to RT. The suppression in generation-recombination noise at 77 K is assigned to the freezing of trapped charge carriers. However, the elevated noise floor at this temperature is due to the dominance of the avalanche mechanism at a lower voltage of ∼−5 V compared to RT, corroborating well with the temperature-dependent *I*–*V* characteristics. The noise characteristics show a 1/*f* dependence revealing a significant contribution of traps in the avalanche process even at 77 K. Thus, the temperature-dependent LFN

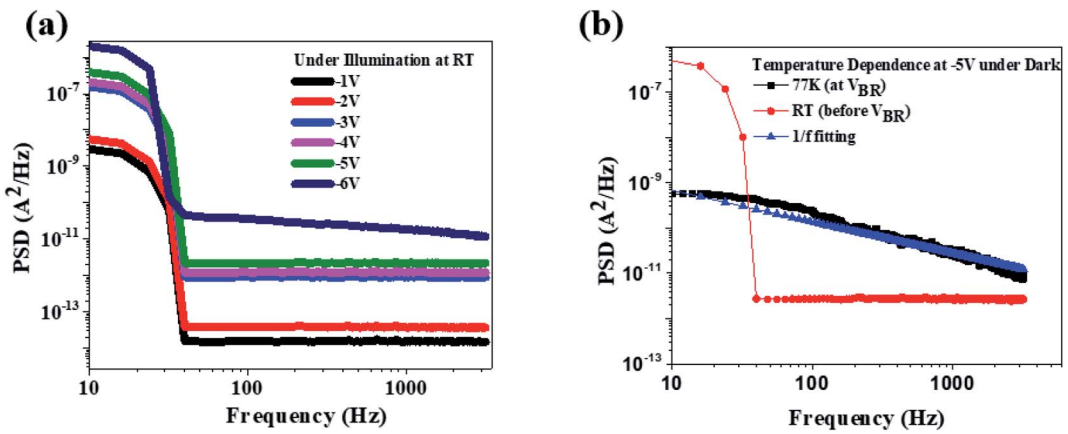

Fig. 7 Ensemble SACM axial NW APD device noise characteristics: (a) under illumination at RT with varying reverse bias, and (b) under dark at −5 V for 77 K and RT.

noise spectroscopy validated the avalanche mechanism in the PD, while the nature and effect of traps' contribution need further study.

The responsivity of these NWs at 1.064 μm was 0.17–0.38 A W^{-1} at the punch-through voltage of ∼−3 V, significantly superior to those reports of Senanayake *et al.*[9] and Farrell *et al.*[11] on patterned vertical ensemble NW APDs thus far. The NW responsivity is limited by the small volume of the absorption region, non-transparent NW contact, lack of antireflection layer on top, and non-uniform nature of ensemble NW growth, which can impact adversely the light trapping features.

The preliminary work on our simple GaAsSb SACM NW APD structure shows great promise to boost the device characteristics by implementing patterned NW arrays, improving the NW contacts, and a suitable annealing scheme to subdue the effect of traps. Further, significant advancements can also be made by exploring other device-engineered architectures, namely, a high-bandgap blocking layer for decreased dark current,[42] dual multiplications regions for improved gain characteristics,[43] and impact ionization engineering.[44]

Conclusion

In this study, we have successfully demonstrated the RT operation of ensemble GaAsSb/GaAs based SACM axial NW APDs grown on non-patterned Si substrates at 1.064 μm wavelength. Detailed *E*-field simulations and growth optimization techniques with optical and electrical characterizations were used to realize axial NW SACM APDs. A monotonous increase in multiplication gains was observed from ∼20 below V_{BR} to ∼700 above V_{BR}. Positive temperature dependence of breakdown voltage ∼ +12.6 mV K^{-1} further confirms avalanche breakdown as the gain mechanism in our SACM NW APDs. *C–V* and temperature-dependent noise characteristics also validated the punch-through voltage values and the presence of avalanche gain mechanism in the NW APDs, determined from the *I–V* characteristics. The ensemble SACM NW APD device demonstrated a broad spectral RT response with cut-off wavelength ∼ 1.2 μm with responsivity ∼ 0.17–0.38 A W^{-1} at −3 V. The *C–V* and LFN analysis indicated the presence of traps, and the V_{BR} shifts were correlated to the trap variation. Therefore, a careful examination of the contact/NW interface, exploration of *in situ* segmental annealing to improve the quality of grown material segments, and investigation of the use of different surface passivation layers to subdue the surface trap effects are important for improving ensemble NW APD device performance.

Conflicts of interest

The authors report no conflict of interest in this work.

Acknowledgements

This work is primarily based upon research supported by the National Science Foundation (NSF) under grant no. 1832117. We also thank Dr Joe Campbell (UVA) and Dr Richard Mirin (NIST) for helpful discussions. This work was performed at the Joint School of Nanoscience and Nanoengineering, a member of the Southeastern Nanotechnology Infrastructure Corridor (SENIC) and National Nanotechnology Coordinated Infrastructure (NNCI), which is supported by the National Science Foundation (ECCS-1542174).

References

1 R. R. LaPierre, *et al.*, A review of III–V nanowire infrared photodetectors and sensors, *J. Phys. D: Appl. Phys.*, 2017, **50**(12), 123001.
2 K. Tomioka, *et al.*, Selective-area growth of III-V nanowires and their applications, *J. Mater. Res.*, 2011, **26**(17), 2127–2141.
3 D. Ma, *Avalanche photodiodes arrays.* 2004.
4 A. H. Jones, *et al.*, Low-noise high-temperature AlInAsSb/GaSb avalanche photodiodes for 2-μm applications, *Nat. Photonics*, 2020, **14**(9), 559–563.
5 X. Yi, *et al.*, Extremely low excess noise and high sensitivity AlAs0.56Sb0.44 avalanche photodiodes, *Nat. Photonics*, 2019, **13**(10), 683–686.
6 A. Dehzangi, J. Li and M. Razeghi, Band-structure-engineered high-gain LWIR photodetector based on a type-II superlattice, *Light: Sci. Appl.*, 2021, **10**(1), 17.
7 Y. Zhang, *et al.*, III–V nanowires and nanowire optoelectronic devices, *J. Phys. D: Appl. Phys.*, 2015, **48**, 46.
8 G. Bulgarini, *et al.*, Avalanche amplification of a single exciton in a semiconductor nanowire, *Nat. Photonics*, 2012, **6**(7), 455–458.
9 P. Senanayake, *et al.*, Thin 3D multiplication regions in plasmonically enhanced nanopillar avalanche detectors, *Nano Lett.*, 2012, **12**(12), 6448–6452.
10 L. C. Chuang, *et al.*, GaAs-based nanoneedle light emitting diode and avalanche photodiode monolithically integrated on a silicon substrate, *Nano Lett.*, 2011, **11**(2), 385–390.
11 A. C. Farrell, *et al.*, Plasmonic field confinement for separate absorption-multiplication in InGaAs nanopillar avalanche photodiodes, *Sci. Rep.*, 2015, **5**, 17580.
12 A. C. Farrell, *et al.*, InGaAs-GaAs Nanowire Avalanche Photodiodes Toward Single-Photon Detection in Free-Running Mode, *Nano Lett.*, 2019, **19**(1), 582–590.
13 V. Jain, *et al.*, InP/InAsP Nanowire-Based Spatially Separate Absorption and Multiplication Avalanche Photodetectors, *ACS Photonics*, 2017, **4**(11), 2693–2698.
14 S. J. Gibson, *et al.*, Tapered InP nanowire arrays for efficient broadband high-speed single-photon detection, *Nat. Nanotechnol.*, 2019, **14**(5), 473–479.
15 E. Alarcon-Llado, *et al.*, Raman spectroscopy of self-catalyzed GaAs(1-x)Sb(x) nanowires grown on silicon, *Nanotechnology*, 2013, **24**(40), 405707.
16 S. Conesa-Boj, *et al.*, Gold-free ternary III-V antimonide nanowire arrays on silicon: twin-free down to the first bilayer, *Nano Lett.*, 2014, **14**(1), 326–332.
17 L. Li, *et al.*, Near Full-Composition-Range High-Quality GaAs1-xSbx Nanowires Grown by Molecular-Beam Epitaxy, *Nano Lett.*, 2017, **17**(2), 622–630.

18 E. Ahmad, *et al.*, Bandgap tuning in GaAs1–xSbx axial nanowires grown by Ga-assisted molecular beam epitaxy, *Semicond. Sci. Technol.*, 2017, **32.3**, 035002.
19 P. K. Kasanaboina, *et al.*, Tailoring of GaAs/GaAsSb core-shell structured nanowires for IR photodetector applications, *Quantum Dots and Nanostructures: Synthesis, Characterization, and Modeling XII*, SPIE, vol. 9373, 2015.
20 E. Ahmad, *et al.*, Te incorporation in GaAs1–xSbx nanowires and pin axial structure, *Semicond. Sci. Technol.*, 2016, **31.12**, 125001.
21 P. K. Kasanaboina, *et al.*, Bandgap tuning of GaAs/GaAsSb core-shell nanowires grown by molecular beam epitaxy, *Semicond. Sci. Technol.*, 2015, **30.10**, 105036.
22 P. Ramaswamy, *et al.*, Be-doping assessment in Self-Catalyzed MBE Grown GaAs Nanowires, *CLEO: Science and Innovations*, Optical Society of America, 2021.
23 M. Parakh, *et al.*, Corrigendum: Space charge limited conduction mechanism in GaAsSb nanowires and the effect of in-situ annealing in ultra-high vacuum, *Nanotechnology*, 2020, **31**, 025205.
24 R. Pokharel, *et al.*, Epitaxial High-Yield Intrinsic and Te-Doped Dilute Nitride GaAsSbN Nanowire Heterostructure and Ensemble Photodetector Application, *ACS Appl. Electron. Mater.*, 2020, **2**(9), 2730–2738.
25 K. Tomioka, *et al.*, Selective-area growth of vertically aligned GaAs and GaAs/AlGaAs core-shell nanowires on Si(111) substrate, *Nanotechnology*, 2009, **20**(14), 145302.
26 M. A. Khamis, *et al.*, Effect of Multiplication and Absorption Layers Width on Avalanche Multiplication Gain in InGaAs/InP Avalanche Photodiode, *Int. J. Eng. Technol.*, 2018, **7**(4.35), 559–563.
27 P. Kleinow, *et al.*, Experimental investigation of the charge-layer doping level in InGaAs/InAlAs avalanche photodiodes, *Infrared Phys. Technol.*, 2015, **71**, 298–302.
28 H. Shu, *et al.*, Impact of Surface Point Defects on Electronic Properties and p-Type Doping of GaAs Nanowires, *J. Phys. Chem. C*, 2016, **120**(38), 22088–22095.
29 S. K. Ojha, *et al.*, Incorporation of Be dopant in GaAs core and core–shell nanowires by molecular beam epitaxy, *J. Vac. Sci. Technol., B: Nanotechnol. Microelectron.: Mater., Process., Meas., Phenom.*, 2016, **34**, 2.
30 E. A. Anyebe, *et al.*, Surfactant effect of antimony addition to the morphology of self-catalyzed InAs1–x Sb x nanowires, *Nano Res.*, 2014, **8**(4), 1309–1319.
31 L. Zhang, H. F. Tang and T. F. Kuech, Effect of Sb as a surfactant during the lateral epitaxial overgrowth of GaN by metalorganic vapor phase epitaxy, *Appl. Phys. Lett.*, 2001, **79.19**, 3059–3061.
32 E. Koivusalo, *et al.*, The role of As species in self-catalyzed growth of GaAs and GaAsSb nanowires, *Nanotechnology*, 2020, **31.46**, 465601.
33 M. Hakala, M. J. Puska and R. M. Nieminen, Native defects and self-diffusion in GaSb, *J. Appl. Phys.*, 2002, **91**(8), 4988–4994.
34 C. Yang, *et al.*, Single p-type/intrinsic/n-type silicon nanowires as nanoscale avalanche photodetectors, *Nano Lett.*, 2006, **6**(12), 2929–2934.
35 S. R. Bank, *et al.*, Avalanche Photodiodes Based on the AlInAsSb Materials System, *IEEE J. Sel. Top. Quantum Electron.*, 2018, **24**(2), 1–7.
36 A. C. Farrell, *et al.*, Diode Characteristics Approaching Bulk Limits in GaAs Nanowire Array Photodetectors, *Nano Lett.*, 2017, **17**(4), 2420–2425.
37 P. Yuan, *et al.*, Avalanche photodiodes with an impact-ionization-engineered multiplication region, *IEEE Photonics Technol. Lett.*, 2000, **12**(10), 1370–1372.
38 R. J. McIntyre, Multiplication noise in uniform avalanche diodes, *IEEE Trans. Electron Devices*, 1966, **ED-13**(1), 164–168.
39 O. Hayden, R. Agarwal and C. M. Lieber, Nanoscale avalanche photodiodes for highly sensitive and spatially resolved photon detection, *Nat. Mater.*, 2006, **5**(5), 352–356.
40 S. Devkota, *et al.*, A study of n-doping in self-catalyzed GaAsSb nanowires using GaTe dopant source and ensemble nanowire near-infrared photodetector, *Nanotechnology*, 2020, **31**(50), 505203.
41 R. Joly, *et al.*, Evidence of Negative Capacitance and Capacitance Modulation by Light and Mechanical Stimuli in Pt/ZnO/Pt Schottky Junctions, *Sensors*, 2021, **21**, 6.
42 M. Nouri and A. Ghadimi, Reduction of dark current and gain increase in InAs avalanche photodiode with AlGaAs blocking layer, *Optik*, 2017, **148**, 268–274.
43 Z. Ahmad, *et al.*, High-Power and High-Responsivity Avalanche Photodiodes for Self-Heterodyne FMCW Lidar System Applications, *IEEE Access*, 2021, **9**, 85661–85671.
44 M. E. Woodson, *et al.*, Low-noise AlInAsSb avalanche photodiode, *Appl. Phys. Lett.*, 2016, **108**(8), 081102.